

Assessing the importance of multicomponent transport properties in direct numerical simulations of premixed, turbulent flames using an efficient, dynamic memory algorithm

Aaron J. Fillo^a, Jason Schlup^b, Guillaume Blanquart^c, Kyle E. Niemeyer^{a,*}

^a*School of Mechanical, Industrial, and Manufacturing Engineering, Oregon State University, Corvallis, OR 97331, USA*

^b*Graduate Aerospace Laboratories, California Institute of Technology, Pasadena, CA USA*

^c*Mechanical Engineering, California Institute of Technology, Pasadena, CA, USA*

Abstract

Implementing multicomponent diffusion models in numerical combustion studies is computationally expensive due to the challenges involved in computing diffusion coefficients. As a result, mixture-averaged diffusion treatments are used to avoid these costs. However, to the authors' knowledge, the accuracy and appropriateness of the mixture-averaged diffusion models has not been verified for three-dimensional turbulent premixed flames. This study will evaluate the role of multicomponent mass diffusion in premixed, high-Karlovitz hydrogen flames, neglecting secondary Soret and Dufour effects. Direct numerical simulation (DNS) of these flames is performed by implementing the Stefan–Maxwell equations in NGA. A semi-implicit algorithm decreases computational expense of inverting the full multicomponent ordinary diffusion array while maintaining simulation accuracy and fidelity. The algorithm is unconditionally stable provided the components of the mixture-averaged and multicomponent diffusion coefficient matrices are of order one over the number of species or smaller, and performance scales approximately with the number of species squared. One-dimensional simulations of premixed hydrogen flames are performed and com-

*Corresponding author

Email address: kyle.niemeyer@oregonstate.edu (Kyle E. Niemeyer)

pared with matching cases in Cantera to verify this method. Premixed two-dimensional, unstable and three-dimensional, turbulent hydrogen flames are simulated and compared with previous mixture-averaged DNS results. Simulation conditions are carefully selected to match previously published results and ensure valid comparison. A priori analysis shows similar relative angles between the species diffusion flux vectors and the species gradient vectors between mixture-averaged and multicomponent results. Further, a posteriori analysis demonstrates negligible differences in conditional means of the fuel mass fraction and its diffusion source term against temperature for mixture-average and multicomponent transport, respectively, between the two cases.

Keywords: Turbulent flames, Direct numerical simulation, Multicomponent diffusion, Mixture-averaged diffusion

1. Introduction

Mixture-averaged diffusion models are commonly used to reduce the high computational expense associated with numerical combustion studies [1]. This approach reduces the complexity of the system of equations by approximating the full multicomponent diffusion coefficient matrix as a single diagonal, which significantly reduces the cost of matrix inversion [2]. Several approaches, such as those used by Warnatz [3] and Coltrin et al. [4], reduce the system's complexity even further by approximating multicomponent diffusion processes in terms of equivalent Fickian processes. However, to our knowledge, the accuracy and appropriateness of mixture-averaged approximations has not been evaluated for three-dimensional turbulent flame simulations, despite its common use.

As further motivation for this study, Lapointe and Blanquart [5] recently investigated the impact of differential diffusion on simulations using unity- and nonunity-Lewis number approximations. They reported that methane, *n*-heptane, isooctane, and toluene flames have similar normalized turbulent flame speeds and fuel burning rates when differential diffusion is neglected but that flames using the non-unity Lewis number approximation underpredict the nor-

malized flame speed when including differential diffusion due to reduced burning rates [5]. Similar work by Schlup and Blanquart [6] examined the impact of multicomponent thermal diffusion on DNS of turbulent, premixed, high-Karlovitz hydrogen/air flames. Their results demonstrated that simulations using the mixture-averaged thermal diffusion underpredicted the normalized flame speeds measured for simulations using full multicomponent thermal diffusion. In addition, including multicomponent thermal diffusion resulted in increased production of chemical source terms in regions of high positive curvature. These observed discrepancies between similar flame simulations with different diffusion models warrant a detailed investigation of the fundamental transport phenomena involved.

While data from three-dimensional reacting flow simulations with multicomponent transport are sparse, several studies have investigated the effects of multicomponent transport in simpler configurations. These studies include one-dimensional [7–11] and two-dimensional flames [12] of various unburnt conditions. These works compared the multicomponent model with various levels of diffusion and transport property models (from constant Lewis number to mixture-averaged properties). In general, only minor errors exist between multicomponent and mixture-averaged formulations, especially in simplified flame configurations, such as unstretched laminar flames.

Giovangigli [13] demonstrated that multicomponent Soret effects significantly impact a wide range of laminar hydrogen/air flames. Specifically, they noted that multicomponent Soret effects influenced laminar flame speeds and extinction stretch rates for flat and strained premixed flames, respectively. For high-pressure systems, Borchesi and Bellan [14] developed and analyzed a multi-species turbulent mixing model for large eddy simulations. They focused on turbulent crossflow mixing of a five-species combustion-relevant mixture of *n*-heptane, O₂, CO₂, N₂, and H₂O. This analysis showed that the multi-species transport model significantly improved the accuracy and fidelity of the solution throughout the mixing layer; however, this study only considered non-reacting flows and, as a result, did not assess the impact of multicomponent transport

on the chemistry inherent in turbulent combustion.

Motivated by the dearth of affordable three-dimensional multicomponent transport models, Ern and Giovangigli [9, 15, 16] developed the computationally efficient Fortran library EGLIB for accurately determining transport coefficients in gas mixtures. More recently, Ambikasaran and Narayanaswamy [17] proposed an efficient algorithm to compute multicomponent diffusion velocities, which scales linearly with the number of species. This significant reduces computational cost compared with previous methods that directly invert the Stephan–Maxwell equations and scale with the number of species cubed. Although these libraries provide a significant reduction in the computational cost of determining the multicomponent diffusion coefficients, they fail to provide a method for reducing the large memory requirements for multidimensional simulations using multicomponent diffusion.

These studies provide compelling evidence that multicomponent transport is important and can affect the accuracy of combustion models. However, none assessed how multicomponent transport impacts three-dimensional turbulent systems with detailed chemistry.

In this article, we demonstrate and analyze an efficient, dynamic algorithm that reduces the computational expense of calculating the multicomponent diffusion fluxes. In addition, we present an a priori and a posteriori assessment of the importance of multicomponent transport using direct numerical simulation (DNS) of turbulent hydrogen/air flames. We simulate freely propagating one-dimensional; two-dimensional unsteady; and three-dimensional, turbulent premixed flames, and perform a priori analysis of the relative direction and magnitude of species flux vectors to assess the relative differences between mixture-averaged and multicomponent mass diffusion transport. Finally, we provide an a posteriori assessment of how mixture-averaged and multicomponent mass diffusion transport impact the turbulent statistics of the three-dimensional hydrogen simulation.

2. Governing equations

This section presents the governing equations for variable-density, low-Mach number reacting flows used in this study. In addition, this section outlines the method used to determine the mass diffusion fluxes for both the mixture-averaged and multicomponent approaches, abbreviated here as MA and MC respectively.

2.1. Low Mach-number equations

The variable-density, low-Mach number, reacting flow equations are solved [18, 19]. The conservation equations are:

$$\frac{\partial \rho}{\partial t} + \nabla \cdot \rho \mathbf{u} = 0, \quad (1)$$

$$\frac{\partial \rho \mathbf{u}}{\partial t} + \nabla \cdot (\rho \mathbf{u} \otimes \mathbf{u}) = -\nabla p + \nabla \cdot \boldsymbol{\tau}, \quad (2)$$

$$\frac{\partial \rho T}{\partial t} + \nabla \cdot (\rho \mathbf{u} T) = \nabla \cdot (\rho \alpha \nabla T) + \rho \dot{\omega}_T - \frac{1}{c_p} \sum_i c_{p,i} \mathbf{j}_i \cdot \nabla T + \frac{\rho \alpha}{c_p} \nabla c_p \cdot \nabla T, \quad (3)$$

$$\frac{\partial \rho Y_i}{\partial t} + \nabla \cdot (\rho \mathbf{u} Y_i) = -\nabla \cdot \mathbf{j}_i + \dot{\omega}_i, \quad (4)$$

where ρ is the mixture density, \mathbf{u} is the velocity, p is the hydrodynamic pressure, $\boldsymbol{\tau}$ is the viscous stress tensor, T is the temperature, α is the mixture thermal diffusivity, $c_{p,i}$ is the constant-pressure specific heat of species i , c_p is the constant-pressure specific heat of the mixture, \mathbf{j}_i is the diffusion flux of species i , Y_i is the mass fraction of species i , and $\dot{\omega}_i$ is the production rate of species i . In Eq. (3), the temperature source term $\dot{\omega}_T$ is given by

$$\dot{\omega}_T = -c_p^{-1} \sum_i h_i(T) \dot{\omega}_i, \quad (5)$$

where $h_i(T)$ is the specific enthalpy of species i as a function of temperature. Similarly, the density is determined from the ideal gas equation of state

$$\rho = \frac{P_o W}{RT}, \quad (6)$$

where P_o is the thermodynamic pressure, R is the universal gas constant, and W is the mixture molecular weight determined via $W = [\sum_i Y_i / W_i]^{-1}$ where W_i is the molar mass of the i th species.

The diffusion fluxes are calculated with either the mixture-averaged [2] or multicomponent [20] models, which are both based on Boltzmann’s equation for the kinetic theory of gases [20, 21]. The baro-diffusion term is commonly neglected in reacting flow simulations under the low Mach-number approximation [22]. We have also neglected thermal diffusion because our objective in this work is to investigate the impact of mass diffusion models; Schlup and Blanquart [6, 23] previously explored the effects of thermal diffusion modeling.

2.2. Mixture-averaged (MA) species diffusion flux

The i th species diffusion flux for the mixture-averaged diffusion model is related to the species gradients by a Fickian formulation and is expressed as

$$\mathbf{j}_i = \rho D_{i,m} \frac{Y_i}{X_i} \nabla X_i - \rho Y_i \mathbf{u}'_c, \quad (7)$$

where X_i is the i th species mole fraction, $D_{i,m}$ is the i th species mixture-averaged diffusion coefficient as expressed by Bird et al. [2]:

$$D_{i,m} = \frac{1 - Y_i}{\sum_{i \neq j}^N X_j / \mathcal{D}_{ji}}, \quad (8)$$

where \mathcal{D}_{ji} is the binary diffusion coefficient between the i th and j th species N is the total number of species. Finally, \mathbf{u}'_c is the correction velocity used to ensure mass continuity requires a sum over the number of species, N :

$$\mathbf{u}'_c = - \sum_i^N \rho D_{i,m} \frac{Y_i}{X_i} \nabla X_i. \quad (9)$$

The expression for species diffusion flux can be re-stated in terms of mass fraction Y_i as

$$\mathbf{j}_i = \rho D_{i,m} \left(\sum_j^N \nabla Y_j \frac{W}{W_j} - \nabla Y_i \right) - \rho Y_i \mathbf{u}'_c, \quad (10)$$

where $D_{i,m}$ corresponds to the i th diagonal element of the mixture-averaged diffusion coefficient matrix, defined herein as \mathbf{D}^{MA} .

2.3. Multicomponent (MC) species diffusion flux

The multicomponent diffusion model for the i th species diffusion flux is

$$\mathbf{j}_i = \frac{\rho Y_i}{X_i W} \sum_{i \neq k}^N W_j D_{ij} \nabla X_j \quad (11)$$

and can be re-stated in terms of the mass fraction as

$$\mathbf{j}_i = \rho \sum_k -D_{ik}^{\text{MC}} \nabla Y_k, \quad (12)$$

where

$$D_{ik}^{\text{MC}} = -\frac{W_i}{W} \sum_{i \neq k}^N \left[D_{ik} - \frac{W}{W_k} \left(\sum_j D_{ij} Y_j \right) \right], \quad (13)$$

W_j is the molar mass of the j th species, and D_{ik} is the ordinary multicomponent diffusion coefficient (computed using the `MCMDIF` subroutine of CHEMKIN II [24] with the method outlined by Dixon-Lewis [25]). The diagonal of the ordinary multicomponent diffusion matrix, D_{ii} , is zero. This approach computes the multicomponent diffusion coefficients, thermal conductivities, and thermal diffusion coefficients from the solution of a system of equations defined by the L matrix and is composed of nine sub-matrices:

$$\begin{bmatrix} \mathbf{L}^{00,00} & \mathbf{L}^{00,10} & 0 \\ \mathbf{L}^{10,00} & \mathbf{L}^{10,10} & \mathbf{L}^{10,01} \\ 0 & \mathbf{L}^{01,10} & \mathbf{L}^{01,01} \end{bmatrix} \begin{bmatrix} \mathbf{a}_1^{00} \\ \mathbf{a}_1^{10} \\ \mathbf{a}_1^{01} \end{bmatrix} = \begin{bmatrix} 0 \\ \mathbf{X} \\ \mathbf{X} \end{bmatrix}, \quad (14)$$

where the right-hand side is composed of the one-dimensional mole fraction arrays \mathbf{X} . From this system of equations, the inverse of the $\mathbf{L}^{00,00}$ block provides the multicomponent diffusion coefficients:

$$D_{ij} = X_i \frac{16T}{25P} \frac{W}{W_j} (q_{ij} - q_{ii}), \quad (15)$$

where

$$\mathbf{q} = (\mathbf{L}^{00,00})^{-1}. \quad (16)$$

The $\mathbf{L}^{00,00}$ sub-matrix block is given by

$$L_{ij}^{00,00} = \frac{16T}{25P} \sum_{k=1}^N \frac{X_k}{W_i \mathcal{D}_{ik}} \{W_j X_j (1 - \delta_{ik}) - W_i X_i (\delta_{ij} - \delta_{jk})\}, \quad (17)$$

where δ_{ij} is the reduced dipole moment of the j th species.

3. Methods

As discussed previously, multicomponent mass diffusion has not yet been incorporated into three-dimensional turbulent flame simulations due to its high computational expense. This section presents the discretized equations, numerical algorithm, and preconditioner proposed. The method is based on the semi-implicit time-marching scheme for species mass fraction fields proposed by Savard et al. [19].

3.1. Multicomponent model implementation

This work was completed using the structured, multi-physics, and multi-scale finite-difference code NGA [18, 19]. NGA is suitable for a wide range of problems, including laminar and turbulent flows [26–28], constant- and variable-density flows [18, 29, 30], large eddy simulation (LES) [27, 31], and direct numerical simulation (DNS) [29, 30, 32]. NGA discretely conserves mass, momentum, and kinetic energy with an arbitrarily high-order spatial accuracy [18].

NGA’s variable-density flow solver uses both spatially and temporally staggered variables, storing all scalar quantities (ρ , P , T , Y_i) at the volume centers and velocity components at their respective volume faces [18, 33]. The convective term in the species transport equation is discretized using the bounded, quadratic, upwind biased, interpolative convective scheme (BQUICK) [34]. The diffusion source term is discretized using a second-order centered scheme and the variables are advanced in time using a second-order semi-implicit Crank–Nicolson scheme [35].

An iterative procedure is applied to fully cover the nonlinearities in the Navier–Stokes equations and the species diffusion terms. Prior studies demonstrated this iterative process to be critically important for stability and accuracy [18, 19, 35, 36]. Savard et al. [19] fully detailed the numerical algorithm sequence; this method is summarized here. This summary is independent of the preconditioning strategy employed in NGA. For clarity, the chemical source terms are integrated explicitly in the following summary; in practice the chemical source terms are also integrated semi-implicitly using the method developed

by Savard et al. [19]. We describe the proposed modifications to NGA’s preconditioning strategy in Section 3.2.

A uniform time step Δt is used. The density, pressure, and scalar fields are advanced from time level $t^{n+1/2}$ to $t^{n+2/3}$, and the velocity fields are advanced from time t^n to t^{n+1} , where t^n is the current time. A total number of iterations, Q , are assumed; each sub-iteration follows the following procedure:

0. Upon convergence of the previous time step, the density, pressure, velocity, and scalar fields are stored. The solutions for pressure, species mass fraction, and momentum (from the previous time step) are used as an initial guess for the iterative procedure, ensuring that continuity is satisfied at the start of the iterative procedure. An Adams–Bashforth prediction is used for the initial density evaluation

$$\rho_0^{n+3/2} = 2\rho^{n+1/2} - \rho^{n-1/2} , \quad (18)$$

this ensures that the continuity equation is discretely satisfied at the beginning of the iterative procedure.

1. For the sub-iterations $k = 1, \dots, Q$, the scalar fields are advanced in time using the semi-implicit Crank–Nicolson method [35, 37]:

$$\begin{aligned} \rho_k^{n+3/2} \mathbf{Y}_{k+1}^{n+3/2} &= \rho^{n+1/2} \mathbf{Y}^{n+1/2} + \Delta t (\mathbf{C}_k^* + \mathbf{Diff}_k^* + \mathbf{\Omega}_k^*) \\ &\quad + \frac{\Delta t}{2} \left(\frac{\partial \mathbf{C}}{\partial \mathbf{Y}} + \frac{\partial \mathbf{Diff}}{\partial \mathbf{Y}} \right)_k^{n+1} \cdot \left(\mathbf{Y}_{k+1}^{n+3/2} - \mathbf{Y}_k^{n+3/2} \right) , \end{aligned} \quad (19)$$

where $\mathbf{Diff} = -\nabla \cdot \mathbf{j}_i$ and \mathbf{Y}_k^* , \mathbf{C}_k^* , \mathbf{Diff}_k^* , and $\mathbf{\Omega}_k^*$ are the mass fraction, convective, diffusive, and chemical terms evaluated on the mid-point (or half time-step) scalar field \mathbf{Y}_k^* and are of the form

$$\mathbf{Y}_k^* = \frac{\mathbf{Y}^{n+1/2} + \mathbf{Y}_k^{n+3/2}}{2} . \quad (20)$$

To simplify the discrete notations for spatial differentiation, the operators corresponding to the convective and diffusive terms in Eq. (4) are written as \mathbf{C} and \mathbf{Diff} , respectively [19]. $\frac{\partial \mathbf{C}}{\partial \mathbf{Y}}$ and $\frac{\partial \mathbf{Diff}}{\partial \mathbf{Y}}$ are the Jacobian matrices corresponding to the convective and diffusive terms with respect

to the species mass fractions, respectively. \mathbf{C} and $\frac{\partial \mathbf{C}}{\partial \mathbf{Y}}$ are functions of the density and velocity, while \mathbf{Diff} and $\frac{\partial \mathbf{Diff}}{\partial \mathbf{Y}}$ are functions of the density, diffusivity, and molar weight. They are consistently updated at each sub-iteration [19].

2. The density field, $\rho_{k+1}^{n+3/2}$, is evaluated from the new scalar fields using Eq. (6). We do not rescale the scalar fields as proposed by Shunn et al. [36]. However, upon convergence of the sub-iterations, this method is equivalent to the density treatment they proposed [19].
3. A Poisson equation is then solved for the fluctuating hydrodynamic pressure using the HYPRE package [18, 38]. The predicted velocity field is then updated.
4. Upon convergence of the sub-iterations, the solutions are updated.

The procedure summarized above becomes equivalent to the fully implicit Crank–Nicolson time-integration scheme upon convergence of the sub-iterations [35]. Savard et al. [33] describe this method in full detail; we direct readers there for additional information on the underlying iterative procedure used in NGA.

3.2. Preconditioning

Expansion of the above numerical procedure to incorporate multicomponent diffusion is based only on modifying the time-marching step for species mass fraction fields in the method by Savard et al. [19]. Specifically, this method modifies the treatment of the mass-diffusion source term in the species mass fraction fields. All other intermediate steps are unchanged.

3.2.1. Preconditioning iterative method

For simpler implementation, Eq. (19) is solved in its residual form

$$\begin{aligned} & \left[\rho_k^{n+3/2} \mathbf{I} - \Delta t \left(\frac{\partial \mathbf{C}}{\partial \mathbf{Y}} + \frac{\partial \mathbf{Diff}}{\partial \mathbf{Y}} \right)_k^{n+1} \right] \cdot \left(\mathbf{Y}_{k+1}^{n+3/2} - \mathbf{Y}_k^{n+3/2} \right) \\ & = \rho^{n+1/2} \mathbf{Y}^{n+1/2} - \rho_k^{n+3/2} \mathbf{Y}_k^{n+3/2} + \Delta t \left(\mathbf{C}_k^{n+1} + \mathbf{Diff}_k^{n+1} + \mathbf{\Omega}_k^* \right). \end{aligned} \quad (21)$$

This equation can be restated as

$$\mathbf{Y}_{k+1}^{n+3/2} = \mathbf{Y}_k^{n+3/2} - \Delta t \mathbf{J}^{-1} \cdot \Theta_k, \quad (22)$$

where the matrix \mathbf{J} is

$$\mathbf{J} = \rho_k^{n+3/2} \mathbf{I} - \frac{\Delta t}{2} \left(\frac{\partial \mathbf{C}}{\partial \mathbf{Y}} + \frac{\partial \mathbf{Diff}}{\partial \mathbf{Y}} \right)_k^{n+1} \quad (23)$$

and the vector

$$\Theta_k = \frac{\rho_k^{n+3/2} \mathbf{Y}_k^{n+3/2} - \rho_k^{n+1/2} \mathbf{Y}_k^{n+1/2}}{\Delta t} - [(\mathbf{C}_k^{n+1} + \mathbf{Diff}_k^{n+1}) \cdot \mathbf{Y}_k^* + \Omega_k^*] \quad (24)$$

is the residual of the species transport equation at the previous sub-iterations, and asymptotes to zero as the sub-iterations fully converge.

Written in its residual form, the time advancement of the species transport equations described here resembles the standard preconditioned Richardson-type iterative method [19, 39], where the matrix \mathbf{J} acts as a preconditioner. The choice of \mathbf{J} as a preconditioner is arbitrary and only affects the convergence characteristics of the iterative method [19]. For example,

$$\mathbf{J} = \rho_k^{n+3/2} \mathbf{I} \quad (25)$$

is equivalent to fully explicit integration of the convective, diffusive, and chemical source terms in the species transport equations. Alternatively,

$$\mathbf{J} = \rho_k^{n+3/2} \mathbf{I} - \frac{\Delta t}{2} \left(\frac{\partial \mathbf{C}}{\partial \mathbf{Y}} + \frac{\partial \mathbf{Diff}}{\partial \mathbf{Y}} + \frac{\partial \Omega}{\partial \mathbf{Y}} \right)_k^{n+1} \quad (26)$$

is equivalent to fully implicit integration of the convective, diffusive, and chemical source terms [19].

There is a clear trade-off in selecting the preconditioner. Since preconditioning is applied to each step of the iterative methods, the form of matrix \mathbf{J} should be optimized for low computational and inversion cost while maintaining strong convergence. The fully explicit preconditioner provides the cheapest option but in our experience results in poor convergence performance, requiring extremely small time steps. Alternatively, the fully implicit preconditioner would provide excellent convergence criteria and unconditional stability, but would be unfeasible due to high computation cost. Unfortunately, the Jacobian matrices for the chemical and diffusion source terms are typically dense [2, 24, 40], and so constructing the preconditioner will become prohibitively expensive for larger

kinetic models. Thus, constructing the preconditioner may become prohibitively expensive when considering a large number of chemical species.

In an attempt to achieve strong convergence while maintaining a low-cost form for the preconditioner, we propose an approximation of the chemical and diffusion Jacobians that lies between the fully-implicit and fully-explicit extremes: a semi-implicit preconditioner. Savard et al. [19] previously implemented a similar approach for preconditioning the convective and chemical Jacobians. Here we describe an approximation to the full multicomponent diffusion Jacobian.

3.2.2. Semi-implicit preconditioning for multicomponent mass diffusion

In Eq. (26), the Jacobian of the diffusion source term depends on the multicomponent diffusion flux and is proportional to the multicomponent diffusion coefficient matrix, \mathbf{D}^{MC} , and thus \mathbf{D}^{MC} may be a reasonable approximation to the fully implicit Jacobian. Recall that

$$\mathbf{Diff} = -\nabla \cdot \mathbf{j}_i \quad \text{and} \quad \mathbf{j}_i = \rho \sum_k D_{ik}^{\text{MC}} \nabla Y_k. \quad (27)$$

From mass conservation the sum of the fluxes must be zero; knowing that D_{ik}^{MC} is computed from the local species and temperature values, not global changed, it holds that the diffusion coefficients are independent of global gradients.

Similarly, the mixture-averaged diffusion coefficient matrix, \mathbf{D}^{MA} , is also independent of spatial gradients and is itself an approximation of the multicomponent diffusion coefficient matrix, \mathbf{D}^{MC} . The matrices are of similar order and both depend on the underlying species diffusivities. Moreover, since \mathbf{D}^{MA} is strictly diagonal and thus inexpensive to invert, it provides a low-cost approximation to the diffusion Jacobian.

3.3. Dynamic memory algorithm

As mentioned previously, high-fidelity simulations with full multicomponent mass diffusion will have a high computational expense. Thus, to facilitate a cost-effective implementation of full multicomponent diffusion we propose a simple

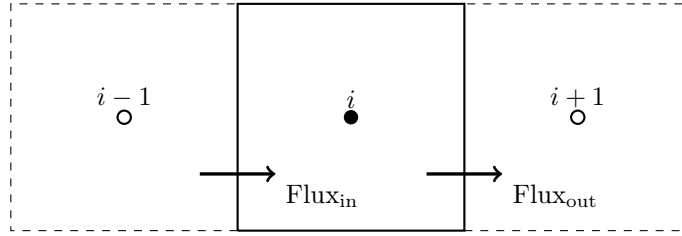
dynamic memory algorithm that significantly reduces the computational resources needed for such simulations.

The cost of simulating full multicomponent diffusion comes from evaluating the \mathbf{D}^{MC} matrix and not the spatial gradients associated with the scalar fields in the conservation equations (3) and (4). Thus, computational cost can be significantly reduced by limiting the evaluation of \mathbf{D}^{MC} to strictly once per grid point. This is possible because the second-order central-difference scheme used is additive and commutative by nature. In other words, the discretized equations are simply added together, and thus the terms are strictly independent of each other and require no information from the surrounding grid points.

Recognizing this, it follows that the order of addition does not matter so long as all of the appropriate terms are included in the discretization. Thus, we can calculate the \mathbf{D}^{MC} matrix once per grid point, and calculate and store for each species the discrete terms of the discretized scalar field corresponding to only the information available at that grid point. The process then repeats at the next grid point and fills in the remaining information. This approach is simply a memory-efficient rearrangement of the floating-point operations and does not alter the final answer. Moreover, this dynamic memory scheme avoids the need to calculate local gradients at each grid point.

In practice, we calculate and store the portions of the enthalpy (Eq. (3)) and species-diffusion source terms (Eq. (4)) that can be computed from the (i) and ($i+1$) flux vectors for a given i, j, k grid point. At the next grid-point ($i+1, j, k$) the process repeats and the remaining information for the previous grid-point (i, j, k) is calculated and stored with half the solution of the next grid-point position. Figure 1 summarizes this process; fluxes are located at cell faces while source terms are at cell centers.

This approach reduces the number of \mathbf{D}^{MC} evaluations from once per species per grid point to strictly once per grid point. Finally, it reduces temporary memory requirements from an array sized $x \times y \times z \times n_{\text{spec}}$ to a 1×6 array. Additional method validation is included in [Appendix A](#).



```

for  $i=1:X$  do
    Calculate diffusion coefficient matrix;
    for  $isc=1:nSpec$  do
        Flux( $i - 1/2$ ) += Fluxin, $isc$ ;
        Flux( $i + 1/2$ ) += Fluxout, $isc$ ;
    end
    Source( $i$ ) += influence from Flux( $i - 1/2$ ) and Flux( $i + 1/2$ ) ;
    Source( $i - 1$ ) += influence from Flux( $i - 1/2$ );
    Source( $i + 1$ ) += influence from Flux( $i + 1/2$ );
end

```

Figure 1: Dynamic algorithm for calculating multicomponent enthalpy and species diffusion source term. Fluxes are located at cell faces while source terms are at cell centers.

4. Test cases

We will evaluate the performance of the proposed iterative method as well as the accuracy and appropriateness of the mixture-averaged diffusion model relative to full multicomponent diffusion in Section 5. We base our evaluation on three flow configurations: a one-dimensional, unstretched, premixed hydrogen/air flame; a two-dimensional, unsteady, laminar, premixed, hydrogen/air flame; and a three-dimensional, statistically stationary, premixed, turbulent hydrogen/air flame. All simulations used the same nine-species hydrogen mechanism of Hong et al. [41] with updated rate constants from the same group [42, 43]. These configurations are described here.

4.1. One-dimensional premixed flame

To ensure accuracy and verify the multicomponent mass-diffusion model, we performed one-dimensional, unstretched (flat), laminar flame simulations and compared these with similar mixture-averaged and multicomponent results computed using Cantera [44]. We selected the one-dimensional flat flame configuration because it restricts all transport to the streamwise direction; this simplifies computation and ensures similar magnitudes in the species source terms for all methods. This is because the spanwise fluxes are zero by definition for this geometry. This similarity may not hold in a multidimensional flow simulation where the multicomponent diffusion fluxes may be misaligned with the species gradient vector. This simplified geometry allows us to directly compare the multicomponent mass diffusion model to the commonly used mixture-averaged diffusion model.

For this comparison we simulated a one-dimensional unstretched (flat) laminar hydrogen/air flame with an equivalence ratio of $\phi = 0.4$ for all Cantera and NGA cases. These simulations used an unburnt temperature of 298 K, pressure of 1 atm, and inlet velocity equal to the laminar flame speed. The flame was centered in the 1.2 cm computational domain with 720 grid points. To ensure fidelity in the results we selected the domain to have at least 20 points through the laminar flame, with the thickness defined using the maximum temperature gradient: $l_F = (T_{\max} - T_{\min})/|\nabla T|_{\max}$. Schlup and Blanquart [6] used an identical configuration to investigate how Soret and Dufour thermal diffusion affects hydrogen-air flames.

The Cantera simulations were similarly run using both mixture-averaged and multicomponent diffusion models with matching inlet conditions, equivalence ratio, and domain size. The freely-propagating adiabatic flat flame solver was used with grid refinement criterion for slope and curve set to 0.1 and a refinement ratio of 2 for 860 grid points. Finally, the Cantera simulations were solved to steady-state with the energy equation enabled.

4.2. Two-dimensional unsteady laminar flame

The two-dimensional domain has inlet and convective outlet boundaries in the streamwise direction and periodic boundaries in the spanwise direction. To keep the unstable flame statistically stationary in the domain, the inlet velocity boundary condition is fixed at the mean effective burning velocity, $S_{\text{eff}}^{2\text{D}}$, defined as

$$S_{\text{eff}}^{2\text{D}} = - \frac{\int_A \rho \dot{\omega}_{\text{H}_2} dA}{\rho_u Y_{\text{H}_2, u} L}, \quad (28)$$

where L is the spanwise dimension of the computational domain. This velocity boundary condition allows us to run the simulation for an arbitrary time to collect statistics.

Table 1 includes details of the computational domain. The physical size of the domain is approximately $120 l_F$ in the streamwise direction by $30 l_F$ in the spanwise direction. The grid is a structured, uniform mesh with 1888×472 cells, with a cell size corresponding to $\Delta x = \Delta y = l_F/16$. The unburnt mixture has an equivalence ratio of $\phi = 0.4$, unburnt temperature of $T_u = 298 \text{ K}$, and unburnt pressure of $p_o = 1 \text{ atm}$. The flame is initialized with an array of solutions corresponding to the one-dimensional flat flame simulations run previously; the flame profile is then initially perturbed in the span-wise direction by two sinusoidal modes. Burali et al. [1] give details of the unstable flame initialization. Figure 2 shows an example temperature contour with a representative unsteady flame clearly visible.

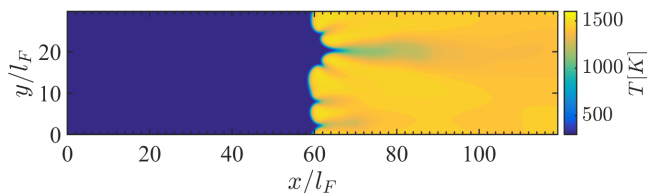


Figure 2: Temperature contour for the two-dimensional freely propagating unsteady hydrogen-air flame obtained with the multicomponent diffusion model.

Table 1: Parameters of the 2D and 3D simulations. Δx is the grid spacing, η_u is Kolmogorov length scale of the unburnt gas, Δt is the simulation time step size, ϕ is the equivalence ratio, T_{peak} is the temperature of peak fuel consumption rate in the one-dimensional laminar flame, S_L is the laminar flame speed, $l_F = (T_b - T_u) / |\nabla T|_{\text{max}}$ is the laminar flame thickness, $l = u'^3 / \epsilon$ is the integral length scale, u' is the turbulence fluctuations, ϵ is the turbulent energy dissipation rate, Ka_u is the Karlovitz number of the unburnt mixture, Re_t is the turbulent Reynolds number of the unburnt mixture, and ν_u is the unburnt kinematic viscosity.

	2D H ₂		3D H ₂	
	MA	MC	MA	MC
Domain	$4L \times L$		$8L \times L \times L$	
L	$472\Delta x$		$190\Delta x$	
Grid	1888×472		$1520 \times 190 \times 190$	
Δx [mm]	0.0424		0.0424	
η_u [m]	—		2.1×10^{-5}	
Δt [s]	5×10^{-6}		6×10^{-7}	
ϕ	0.4		0.4	
T_{peak} [K]	1190	1180	1190	1180
S_L [m/s]	0.230	0.223	0.230	0.223
l_F [mm]	0.643	0.651	0.643	0.631
l/l_F	—		2	2.04
u'/S_L	—		18	18.6
$\text{Ka}_u = \tau_F / \tau_\eta$	—		149	151
$\text{Re}_t = (u'l) / \nu_u$	—		289	

4.3. Three-dimensional flow configuration

As a final test of the multicomponent mass diffusion model and to assess its impact on mass transport, we simulated a three-dimensional, turbulent, premixed, freely propagating flame. The computational domain consists of inflow and convective outflow boundary conditions in the streamwise direction. The two spanwise directions use periodic boundaries. The inflow velocity is the mean turbulent flame speed, which keeps the flame statistically stationary such that turbulent statistics can be collected over an arbitrarily long run time. In the absence of mean shear, we use a linear turbulence-forcing method [29, 45] to maintain the production of turbulent kinetic energy through the flame. Again, the computational setup for this case is similar to those of Burali et al. [1] and Schlup et al. [6], who provide additional configuration details.

The unburnt temperature and pressure are 298 K and 1 atm, respectively. Table 1 provides further details of the computational domain, unburnt mixture, corresponding one-dimensional flames, and inlet turbulence. The inlet equivalence ratio is $\phi = 0.4$, with an unburnt Karlovitz number $\text{Ka}_u = \tau_F/\tau_\eta = 149$, where $\tau_F = l_F/S_L$ is the flame time scale and $\tau_\eta = (\nu_u/\epsilon)^{1/2}$ is the Kolmogorov time scale of the incoming turbulence with unburnt kinematic viscosity ν_i and turbulent energy dissipation ϵ . The unburnt turbulent Reynolds number is $\text{Re}_t = u'l/\nu_u = 289$, where u' is the fluctuation of the mean velocity and l is the integral length scale. The mean inflow velocity at the inlet boundary condition approximately matches the turbulent flame speed so that the flame remains relatively centered in the domain and we can perform arbitrarily long simulations. Once the turbulence has fully developed, the simulations are each run for 25 eddy turnover times, $\tau = k/\epsilon \approx 500 \mu\text{s}$.

The domain has 1520 points in the streamwise direction and 190 points in both spanwise directions, with a uniform grid size of $\Delta x = l_F/16$. This domain is about $100l_F$ in length and $12l_F$ in the spanwise directions; thus, the spanwise dimensions of this case are approximately 40% of the two-dimensional freely propagating dimensions. Given the prescribed turbulence intensity, this mesh has a grid spacing equivalent to $\Delta x \approx 2\eta$, where η is the Kolmogorov length

scale. Figure 3 shows a two-dimensional schematic of the domain, including the locations of the flame and the forcing region. Figure 4 shows a three-dimensional view of the iso-surface of T_{peak} defining the flame front. The flame surface shows the complex behavior of the flame in the turbulent field.

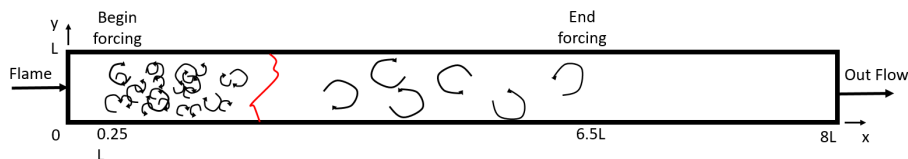


Figure 3: Two-dimensional schematic of the three-dimensional flame configuration. Adapted from Burali et al. and Schlup and Blanquart [1, 6].

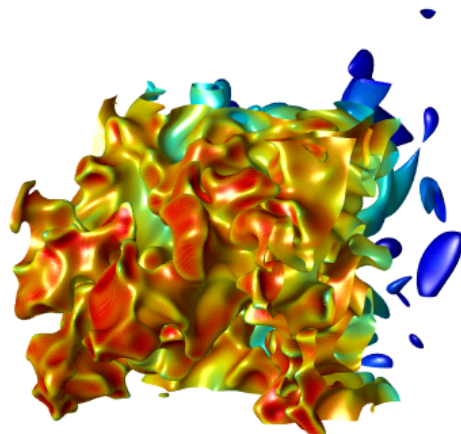


Figure 4: Iso-surface of peak temperature colored by OH mass fraction for a three-dimensional turbulent hydrogen/air flame with multicomponent mass diffusion.

5. Results and discussion

To start, this section presents a theoretical analysis of the stability and convergence of the sub-iterations for the species transport equations. We then present a practical assessment of this convergence, comparing the eigenvalues of

the proposed approximation to the Jacobian matrix with the theoretical analysis. Following this demonstration of the proposed methods stability, we verify the accuracy of the method through a priori and a posteriori assessment of a one-dimensional, unstretched, premixed, laminar flame simulations. Finally, we present an a priori and a posteriori evaluation of the relative differences between the mixture-averaged and multicomponent diffusion models for two-dimensional unsteady and three-dimensional turbulent premixed flame simulations.

5.1. Theoretical stability analysis

To evaluate the theoretical stability of the proposed treatment of the diffusion source terms we will perform a one-dimensional von Neumann stability analysis. We then demonstrate that this one-dimensional analysis does apply to the fully turbulent three-dimensional test case in Section 5.2. Thus, the resulting form of Eq. (21) is transformed into modified wavenumber space by assuming a solution of the form

$$\mathbf{Y}(x, y, z, t) = f(t)e^{i\kappa x}, \quad (29)$$

where κ is the wavenumber and $f(t)$ is the time-varying solution. To simplify the stability analysis, we rewrite Eq. (21) in a point-wise form neglecting both the chemical source term—demonstrated to be stable by Savard et al. [19]—and the convective transport term, which is integrated explicitly (i.e., not modified by sub-iterations). This transforms the N set of partial differential equations (PDEs) into an N set of ordinary differential equations (ODEs), where N is the number of species, such that Eq. (21) reduces to the form

$$\left(\mathbf{I} + \frac{\Delta t}{2} \mathbf{D}^{\text{MA}} \kappa'^2 \right) \left(f_{k+1}^{n+3/2} - f_k^{n+3/2} \right) = f^n - f_k^{n+3/2} + \frac{\Delta t}{2} \mathbf{D}^{\text{MC}} \kappa'^2 \left(f_k^{n+3/2} + f^n \right), \quad (30)$$

where \mathbf{D}^{MA} and \mathbf{D}^{MC} are the mixture-averaged and multicomponent diffusion coefficient matrices calculated from Eqs. (8) and (15) respectively, f^n is the value at the previous time step as defined in step 0 of Section 3.1, and κ' is the

modified wavenumber. For the second-order central differencing scheme used κ' takes the form

$$\kappa'^2 = 2 \left(\frac{1 - \cos(\kappa \Delta x)}{\Delta x^2} \right). \quad (31)$$

While we apply this here to a second-order central difference scheme, this stability analysis holds for any spatial discretization of the diffusion terms in Eq. (21). Dropping the superscripts n and $n + 1$ for clarity, we can reduce Eq. (30) to

$$f_{k+1} = \mathbf{A}f_0 + \mathbf{B}f_k, \quad (32)$$

where

$$\mathbf{A} = \left(\mathbf{I} + \frac{\Delta t}{2} \kappa'^2 \mathbf{D}^{\text{MA}} \right)^{-1} \left(\mathbf{I} + \frac{\Delta t}{2} \kappa'^2 \mathbf{D}^{\text{MC}} \right) \quad (33)$$

and

$$\mathbf{B} = \left(\mathbf{I} + \frac{\Delta t}{2} \kappa'^2 \mathbf{D}^{\text{MA}} \right)^{-1} \left[\frac{\Delta t}{2} \kappa'^2 (\mathbf{D}^{\text{MA}} - \mathbf{D}^{\text{MC}}) \right]. \quad (34)$$

Inspecting Eq. (32), the coefficient \mathbf{A} in front of f_0 is strictly less than one at all points, because \mathbf{D}^{MC} is negative (Eq. (13)). Therefore, the sub-iterations will converge and remain stable if the spectral radius of \mathbf{B} is strictly less than one.

5.2. Practical stability analysis

Using the theoretical stability criterion determined previously, we now analyze the stability of the scheme numerically. While the theoretical analysis was performed assuming explicit transport of the convective terms and constant density and diffusion coefficients, we performed this test case with semi-implicit transport and variable density/diffusion coefficients. It is important to demonstrate the stability of the proposed preconditioner for the semi-implicit multicomponent species diffusion transport in a practical numerical simulation. As we will show, we found the proposed stability criterion to be much less than unity for all test cases.

Figure 5a presents the numerical stability results for the one-dimensional test case. For the time-step size tested, converging (as opposed to converged) sub-iterations implies a stable simulation, which agrees with similar results by

Savard et al. [19]. In other words, unless the sub-iterations diverge, the simulation remains stable. For reference Figure 5b shows the residual of density as a function of sub-iteration, providing an in situ measure of convergence. In Figure 5b the slope of the convergence corresponds to the spectral radius of the diffusion matrix plotted in Figure 5a. Values below 10^{-12} in Figure 5b are nearing machine precision and considered converged. These results suggest that the theory well-approximates actual stability; and correspond to the numerical stability limit for the three-dimensional turbulent premixed flame.

5.3. Accuracy

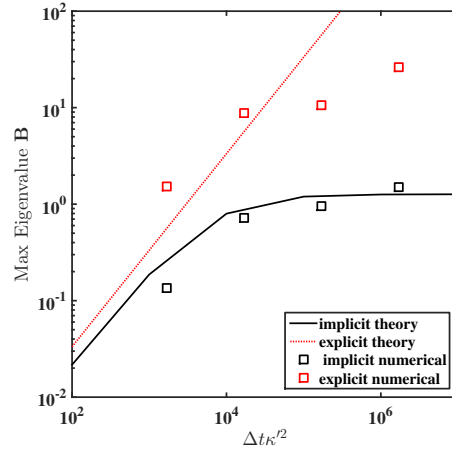
To verify the accuracy of the multicomponent model, we present an a posteriori comparison of the one-dimensional unstretched species profiles and laminar flame speeds. Figure 6 compares the nine species profiles for the steady-state one-dimensional flat flame solutions relative to local mixture temperature for MC and MA from both NGA and Cantera; the profiles all agree within 1% at all points, with the exception of N_2 . The laminar flame speeds (S_L^o) for these simulations are approximately 23.0 cm/s and 22.3 cm/s for the mixture-averaged and multicomponent diffusion NGA cases, respectively. The unstretched laminar flame speed is

$$S_L^o = -\frac{\int \rho \dot{\omega}_{H_2} dx}{\rho_u Y_{H_2,u}}, \quad (35)$$

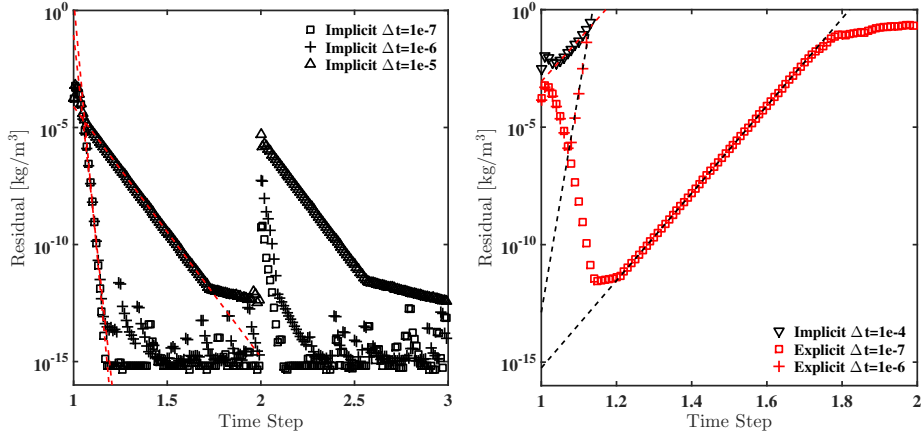
where ρ_u is the unburnt mixture density and $Y_{H_2,u}$ is the unburnt fuel mass fraction. The larger difference in the species profile for N_2 is expected and attributed to the correction velocity term associated with the mixture-averaged diffusion model, which is weighted by mass fraction and thus can heavily impact N_2 due to its high concentration throughout the flame. The strong agreement between the other eight species profiles for both the NGA and Cantera results verifies that the multicomponent model is functional and accurate.

5.4. One-dimensional a priori flux comparison

With the governing physics verified, we next calculated the species flux vectors a priori and independently of the other governing equations to evaluate the



(a) Spectral radius (maximum eigenvalue) of \mathbf{B} as a function of modified wavenumber in the one-dimensional premixed flame for $\Delta t = 2 \times 10^{-6}$.



(b) Stable convergence of density residual for various time step sizes.

(c) Unstable convergence of density residual for various time step sizes.

Figure 5: Numerical stability for proposed method in one-dimensional test case

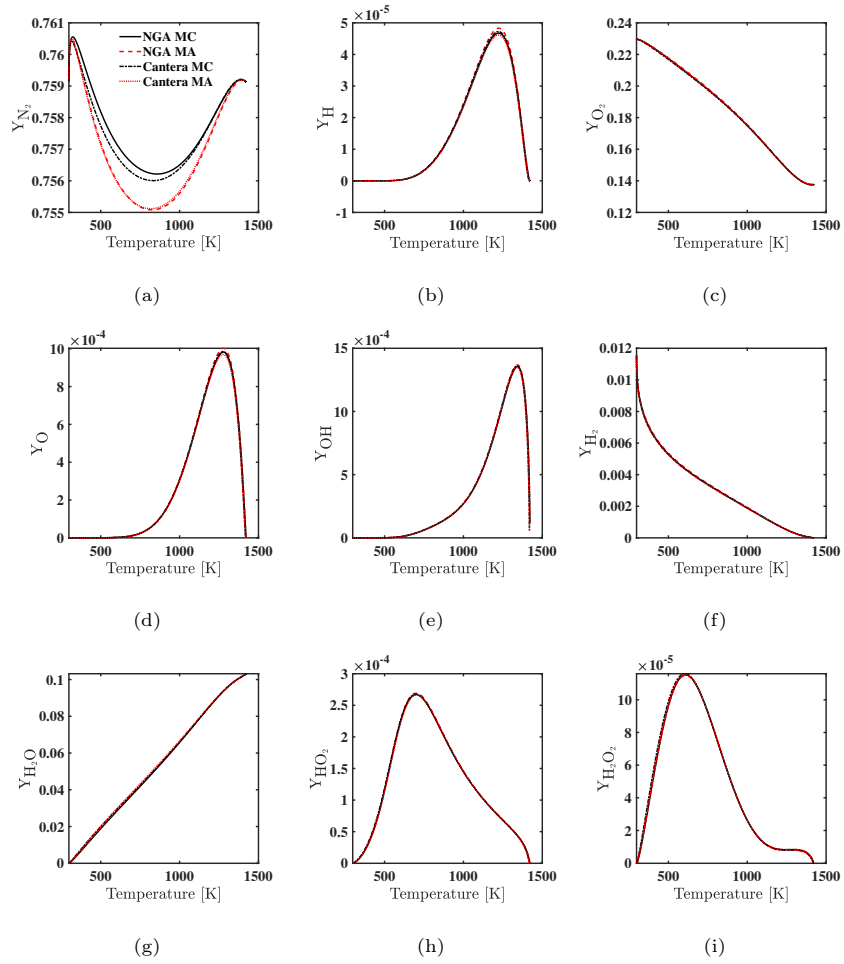


Figure 6: A posteriori comparisons of species mass fractions relative to mixture local temperature in a hydrogen/air flame with $\phi = 0.4$ using NGA and Cantera.

relative accuracy of the mixture-averaged assumption to a full multicomponent implementation in a one-dimensional flow. The fluxes are determined using the same input parameters as stated above for a single time step. In other words, the a priori comparison is based on the same data but evaluated using the different flux equations. It is important that this comparison be performed prior to the initial time-step as the input parameters to the diffusion flux calculation may evolve over time. This a priori comparison provides a one-to-one comparison of the mixture-averaged and multicomponent models before they can be modified by convective transport or global temperature/density gradients.

Figure 7 presents the a priori flux results for all nine chemical species relative to the local mixture temperature. As expected, the flux profiles for the mixture-averaged and multicomponent cases have a similar shape and magnitude. In calculating the magnitude of the species diffusion flux, the mixture averaged model under-predicts the full multicomponent model by as much as 34 % for H, and 18 % for H₂ and OH. We attribute this to the inclusion of the correction velocity to maintain mass continuity in the mixture-averaged model (Eq. (9)). As previously stated, the correction velocity is weighted based on the mole and mass fractions of the species; as a result, a large portion of the correction for mass continuity is lumped into the N₂ mass flux. This weighting of the correction velocity accounts for the observed differences in the flux magnitude for the other species, as presented in Figure 7a. In Figure 7a the maximum magnitude of the N₂ diffusion flux vector for mixture-averaged model is approximately 40 % higher than the multicomponent model; this difference corresponds to the observed differences in the other eight species fluxes and fulfills mass-continuity requirements. As a secondary check, the species mass fluxes for both models sum to zero, confirming that mass is conserved.

5.5. Multi-dimensional assessment of diffusion flux models

This section provides a priori and a posteriori assessments of the species mass diffusion fluxes for two flow configurations. The first is a two-dimensional domain used to study unsteady, freely propagating lean hydrogen/air flames [1, 6].

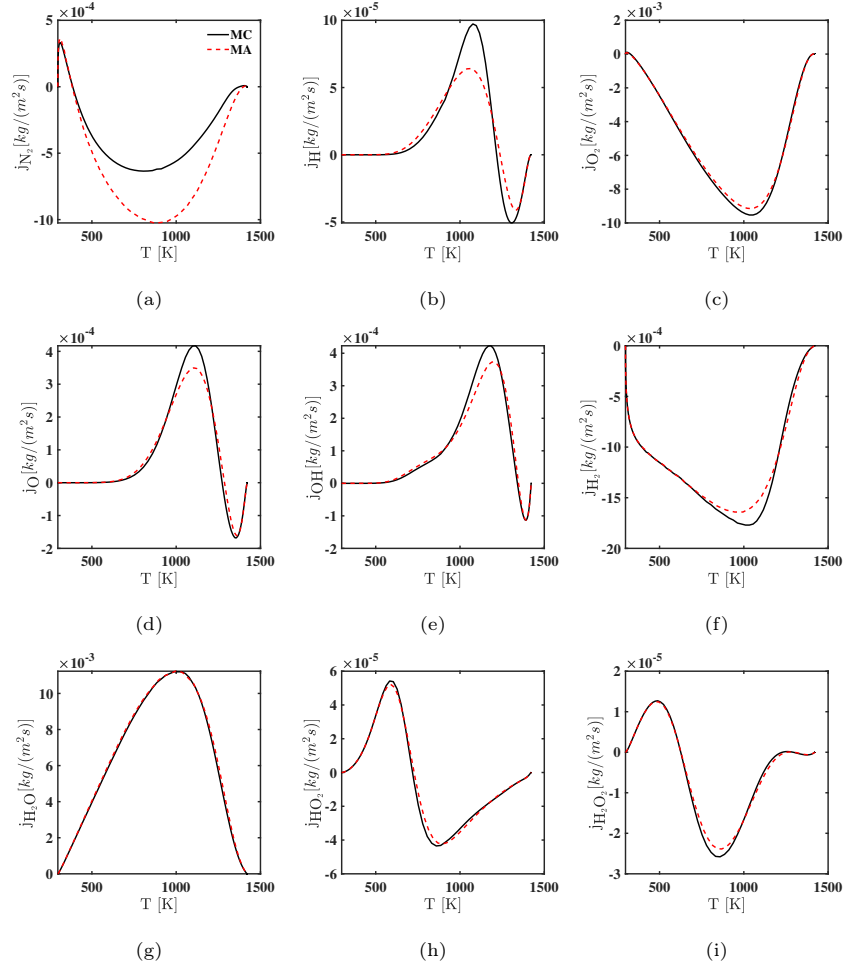


Figure 7: A priori comparisons of mass diffusion fluxes for 9 species hydrogen mechanism relative to mixture local temperature in hydrogen/air flame with $\phi = 0.4$ for NGA.

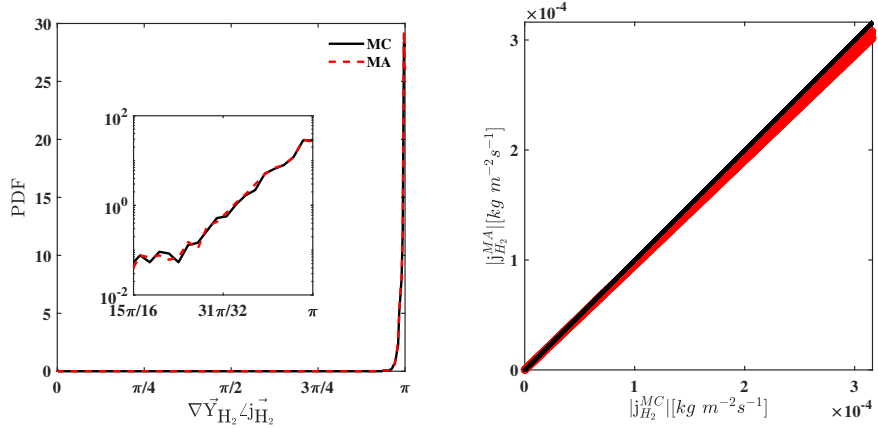
The second configuration is a doubly-periodic domain used to study three-dimensional statistically stationary flames [1, 5, 6]. These configurations represent special cases where diffusion modeling could be important. Differential diffusion effects cause the instabilities found in lean hydrogen/air flames, and at high Karlovitz numbers the turbulence time scales match the order of diffusion time scales. Both flow configurations use the same nine-species hydrogen model with 54 reactions of Hong et al. [41–43] (forward and backward reactions are counted separately).

5.5.1. *A priori diffusion flux comparison*

As with the one-dimensional flames, we performed an a priori assessment of the species mass diffusion fluxes. However, based on the mathematical definitions of the two diffusion models, we now investigate the relative angles of the flux vectors. As demonstrated in Eq. (10), the mixture-averaged flux vector for species i is based on the gradient of that species and, as a result, should be strictly anti-parallel to the species gradient vector. Alternatively, in Eq. (12), the multicomponent flux of species i is based on the net influence of the other $n - 1$ species (but not itself) and thus may not necessarily align with its own species gradient vector.

To assess the impact of the relative diffusion direction, Figure 8a presents a probability density function (PDF) of the angles between the species flux vectors and species gradient vectors for both the mixture-averaged and multicomponent models through the flame front. The a priori analysis is performed using a snapshot from each fuel/air mixture, obtained from the multicomponent simulations; these snapshots are used to evaluate the mass fluxes corresponding to each model. This was done to isolate the effects of the diffusion model from any time-evolution of the reacting flow field. We present the a priori agreement between mixture-averaged and multicomponent diffusion fluxes by comparing their orientation and magnitude. Figure 8 shows the angle PDF for H_2 in the three-dimensional flame. The presented points correspond to points in the domain where the species diffusion flux magnitude is 0.1% of the peak diffusion

flux magnitude; this emphasizes the regions where diffusion is important, i.e., locations of large concentration gradients. The presented results for H_2 represent nine species PDFs for both the two-dimensional unsteady and three-dimensional cases. The PDFs of the angle between species flux and gradient vectors do not differ significantly between the mixture-averaged and multicomponent models.



(a) PDFs of angle between species flux and gradient vectors (semi-log plot in y inset). (b) Mixture-averaged and multicomponent fluxes for H_2 (black line is $y = x$).

Figure 8: A priori assessment of the three-dimensional hydrogen/air mixture-averaged and multicomponent models.

Similarly, Figure 8a plots the mixture-averaged flux magnitudes against those of the multicomponent model for H_2 over the entire domain. At the peak diffusion flux magnitude, the mixture-averaged model matches the multicomponent model within 2%. This result demonstrates that the mixture-averaged diffusion model well-predicts the multicomponent fluxes, though the latter are not strictly anti-parallel to the species gradient vectors.

To provide a qualitative reference, Figure 9 shows a two-dimensional slice of the turbulent hydrogen/air flame near the flame front, colored by the angle between the species gradient and diffusion flux vector for H_2 . The location of the flame is indicated by isolines of $T = T_{\text{peak}} - 400$ K (black) and $T = T_{\text{peak}} + 400$ K (white). Qualitatively, the angles between these two vectors agree well for the

mixture-averaged and multicomponent models. The mixture-averaged fluxes deviate away from π due to the velocity correction term in Eq. (6). Further, these two vectors show a clear preferential alignment at π .

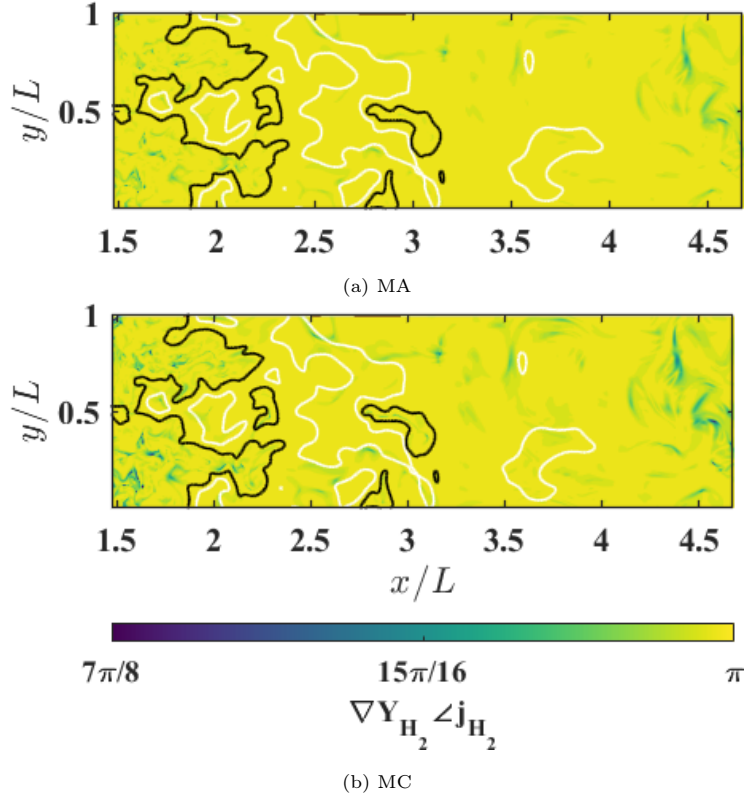


Figure 9: A priori assessment of the three-dimensional hydrogen/air mixture-averaged and multicomponent models comparing two-dimensional slice near the flame front showing the angle between species gradient and diffusion flux vectors (the black and white lines correspond to isosurfaces of $T_{peak}-400$ K and $T_{peak}+400$ K, respectively).

The flux–gradient angles of the mixture-averaged and multicomponent diffusion models share maximums of π , anti-parallel to the species gradient vector; this is expected and indicates that mass primarily diffuses in the direction of negative species gradient (i.e., from high to low concentration). The angle PDFs agree closely between the two models, suggesting that the orientation of the mixture-averaged diffusion flux well-approximates the orientation of the

multicomponent model over the entire range of data.

Figures 8 and 9 demonstrate few observable differences between the mixture-averaged and multicomponent diffusion models for the simulated hydrogen/air flames. Thus, to concisely highlight any minor differences across multiple species and flame configurations, Table 2 presents the mean and standard deviations of the angles between the mixture-averaged and multicomponent diffusion fluxes, as well as relative L^2 error norms of the differences in magnitude of these diffusion fluxes. These statistics are calculated in regions where species diffusion is strong, i.e., where the diffusion flux magnitude is greater than 0.1% of the peak. The relative L^2 error norm for the diffusion flux magnitude of species i is defined as

$$L^2(\mathbf{j}_i^{\text{MA}}) = \sqrt{\frac{\sum_{n=1}^{N_p} \left(\left| \mathbf{j}_i^{\text{MC}} \right| - \left| \mathbf{j}_i^{\text{MA}} \right| \right)^2}{\sum_{n=1}^{N_p} \left| \mathbf{j}_i^{\text{MC}} \right|^2}}, \quad (36)$$

where N_p is the number of points in the domain.

Table 2: Statistical quantities of the mixture-averaged and multicomponent diffusion models for a representative set of major, radical, and product species: the mean (μ_{\angle}) and standard deviation (s_{\angle}) of the angles between the mixture-averaged and multicomponent flux vectors, as well as relative L^2 error norms (Eq. (36)).

	μ_{\angle} [rad]	s_{\angle} [rad]	$L^2(\mathbf{j}_i^{\text{MA}})$
2D unsteady hydrogen			
H ₂	2.7×10^{-5}	2.1×10^{-4}	0.0056
H	5.7×10^{-5}	1.4×10^{-6}	0.024
OH	2.4×10^{-4}	3.2×10^{-5}	0.010
H ₂ O	0.0074	2.1×10^{-4}	0.038
3D hydrogen			
H ₂	0.033	0.073	0.12
H	0.025	0.0051	0.10
OH	7.1×10^{-4}	1.4×10^{-4}	0.023
H ₂ O	0.12	0.0073	0.087

As observed in Table 2, a majority of the mixture-averaged diffusion flux vectors match the multicomponent diffusion flux vectors within a mean an-

gle, μ_{\angle} , of 0.06 rad for the turbulent cases, with negligible differences for the two-dimensional case. For this analysis a mean angle of 0 rad corresponds to alignment of the mixture-averaged and multicomponent flux vectors; i.e. smaller angles represent better agreement. The only exception is the diffusion flux of H₂O for the hydrogen/air turbulent flame with a mean angle of 0.12 rad. As expected, the turbulent cases show larger (albeit still small) values of μ_{\angle} . The effects of turbulence worsens the agreement between the mixture-averaged and multicomponent diffusion flux angles, yet they still remain within ~ 0.1 rad. Additionally, the standard deviations of the angle between the diffusion fluxes, s_{\angle} , are small and of the same order as the mean angles themselves.

Additionally, Table 2 shows that the magnitudes of the diffusion fluxes agree well. Many mixture-averaged diffusion flux magnitudes predict the multicomponent flux magnitudes within a relative error of 0.05, with a maximum relative error of 0.12 for H₂ in the three-dimensional turbulent case. The remaining species show similar trends to those shown here.

5.5.2. *A posteriori comparison of turbulent statistics*

To assess the impact of the observed differences in the relative direction of the species diffusion between the mixture-averaged and multicomponent mass diffusion models, we present an a posteriori comparison of the turbulent statistics. The flames were allowed to develop in a turbulent flow field, and the statistics computed after the initial transients of the initial flow and scalar fields have advected through the domain. As an initial assessment, the effective flame propagation speeds for the two cases were calculated in a similar manner as the two-dimensional freely propagating flames:

$$S_{\text{eff}} = - \frac{\int_V \rho \dot{\omega}_{\text{H}_2} dV}{\rho_u Y_{\text{H}_2, u} L}. \quad (37)$$

Figure 10 shows the time history of the turbulent flame speed over twenty-two eddy turn-over times. The average normalized flame speeds from the mixture-averaged and multicomponent models agree within 14.8 %: $S_T^{\text{MA}}/S_l = 29.6$ and $S_T^{\text{MC}}/S_l^0 = 34.7$, respectively. Although there is a measurable dif-

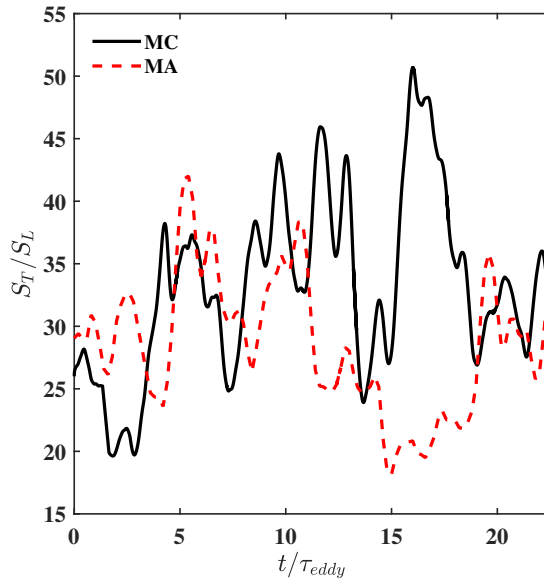


Figure 10: Flame speed history for three-dimensional, freely propagating, premixed, turbulent hydrogen/air flame with $\phi = 0.4$ for 22.5 eddy turnover times.

ference in turbulent flame speed between the two models, the mixture-average model a reasonably approximates of the multicomponent flame speed. This result supports the a priori assessment that the two models are equivalent.

To further assess any differences between the mixture-averaged and multicomponent mass diffusion models, Figure 11 presents the means of fuel mass fraction and its source term conditioned by temperature. As with the turbulent flame speeds, the differences in the calculated conditional means are negligible, (i.e., less than 5.5%). This agreement also extends into super-adiabatic regions for the hydrogen/air flame. These super-adiabatic regions, also called “hot spots”, result from differential diffusion and have been predicted both in theoretical studies [46] and in numerical analyses of lean hydrogen/air mixtures [47–49]. This further demonstrates that while the mixture-averaged and multicomponent models exhibit minor differences in the relative direction and magnitude of the diffusion mass fluxes, these differences do not meaningfully impact the turbulent statistics of the flame.

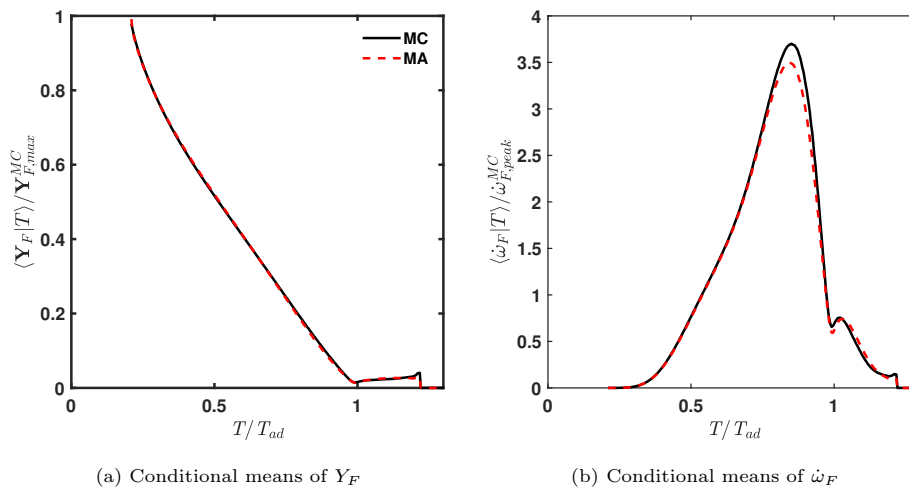


Figure 11: Turbulence statistics for the three-dimensional, freely propagating, premixed, turbulent hydrogen/air flame with $\phi = 0.4$.

5.6. Computational cost

The implemented multicomponent mass diffusion model is computationally efficient. While we do not present a detailed analysis of the computational cost or scaling of the algorithms, a brief discussion of the increased cost to include full multicomponent mass diffusion is necessary to provide context for its use. The presented timing comparisons examine how the method scales with both number of chemical species and spatial dimension.

We tested three chemical kinetic models (containing 9, 35, and 172 species) in a one-dimensional flat flame simulation to determine the cost of multicomponent mass diffusion over a wide range of model sizes. Figure 12 shows the computational time per grid point of computing the diffusion mass fluxes on a desktop workstation. The presented timings include calculation of both the diffusion coefficients and mass diffusion fluxes.

The time taken to compute coefficients for the mixture-averaged model increases quadratically with the number of species. Similarly the time to compute the multicomponent fluxes also scales quadratically with the number of species; however, the multicomponent model does take more time at all points and as

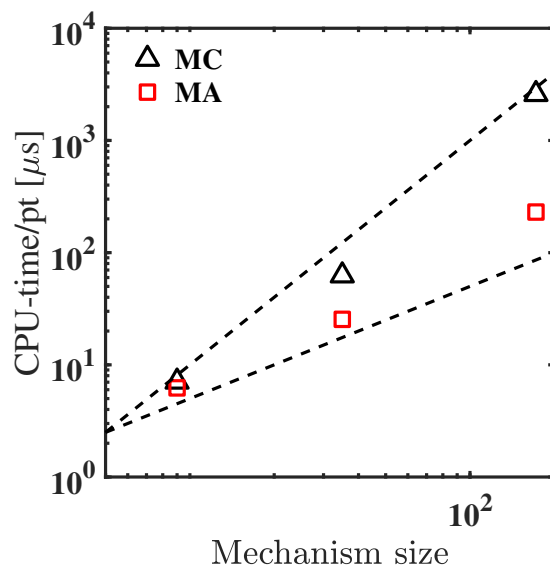


Figure 12: Computational time per grid point of computing diffusion coefficients and diffusion mass fluxes using kinetic models with 9, 35, and 172 species; black dashed lines correspond to linear ($y = x$) and quadratic ($y = x^2$) scaling trends respectively. MC and MA stand for multicomponent and mixture-averaged, respectively.

a result is more expensive. Recall that the multicomponent simulations use CHEMKIN II [24] to determine the ordinary multicomponent diffusion coefficient matrix, which reduces the computational speed; MC and MA would scale similarly if we implemented a more efficient algorithm, such as EGLIB [9, 15, 16].

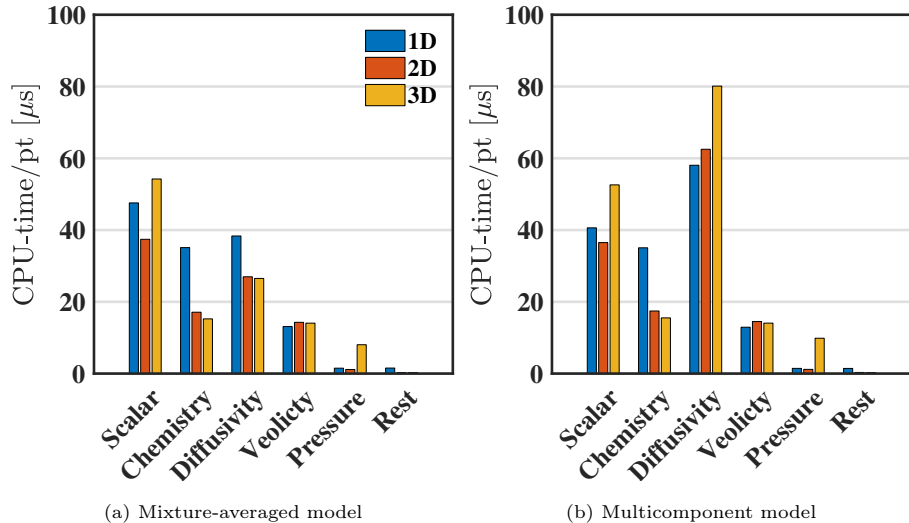


Figure 13: Computational time per grid point for each of the three flame configurations: one-dimensional at (blue), two-dimensional Cartesian (red), and three-dimensional (yellow).

To evaluate how the multicomponent model scales with increasing spatial dimension, we acquired timings for one-, two-, and three-dimensional configurations covering the cases presented in this work; these timing tests were run only for 20 time steps. Figure 12 presents the computational timings, including the time to computer D^{MA} and D^{MC} , for each part of the code for both diffusion models. We performed these computations on the National Energy Research Scientific Computing Center (NERSC) parallel computing cluster Cori (Cray XC40) [50].

While much of the code exhibits a similar cost per grid point, regardless of the dimensionality of the problem, the chemistry is more expensive for one- and two-dimensional cases. This cost increase is due to NGA’s structure. NGA was been written and optimized for three-dimensional configurations, thus the

one- and two-dimensional cases are artificially more expensive, especially in the chemistry calculations.

Consistent with Figure 12, the cost of calculating diffusion (“Diffusivity”) increases with model complexity. Moreover, the multicomponent diffusion mass flux calculation represents roughly 46 % of the total simulation time. Interestingly, cost of diffusion increases only slightly moving from one dimension to two. This results from the high efficiency of the dynamic memory-allocation algorithm used to implement this model. By reducing memory requirements and optimizing calls to memory, the implemented memory algorithm is able to maintain low computational expense. These results indicate that, for hydrogen-air combustion, the multicomponent model is more expensive than the mixture-averaged model; however, the differences in “Diffusivity” between the two models are due to the use of CHEMKIN II [24]. Thus, the slowdown could be resolved by implementing a more-efficient package for calculating the mass diffusion coefficients such as EGLIB [9, 15, 16]; however, the total cost of computing mass diffusion remains notable, even for the mixture-averaged case.

6. Summary and future work

This article proposes an efficient and stable scheme for implementing multicomponent mass diffusion in reacting-flow DNS with minimal memory expense. We assessed the mixture-averaged and multicomponent models for species diffusion using both a priori and a posteriori measures for one-dimensional steady; two-dimensional unsteady; and three-dimensional, turbulent, premixed, freely propagating hydrogen/air flames. We did not observe any notable differences between the two models when comparing the relative direction and magnitude of the flux vectors or turbulent statistics. Although, small difference in the turbulent flame speeds between the two models were observed, the differences in the conditional means of the fuel source term and mass fraction were negligible suggesting the mixture averaged model well approximates full multicomponent diffusion. Finally, the proposed scheme is efficient and stable and exhibits rea-

sonable computational cost for chemical kinetic models smaller than than 100 species; this performance could be further improved by implementation of a more efficient method for calculating the multicomponent diffusion coefficient matrix.

The results presented for hydrogen flames suggest that the mixture-averaged mass diffusion model suffices for DNS of three-dimensional, premixed turbulent flames in the regimes and configurations considered. However, despite these results, we do not have sufficient data to draw firm conclusions on the accuracy and appropriateness of mixture-averaged assumptions for all flames (i.e., all fuels, configurations, and regimes). Additional data are needed from studies of different fuels—namely large hydrocarbons—and kinetic models with more species.

In support of this effort, we are currently performing several three-dimensional turbulent flame DNS for *n*-heptane/air and toluene/air flames. The models for these species include 35 and 47 species, respectively. The three-dimensional turbulent simulations include the full multicomponent diffusion model and will provide a detailed assessment of the mixture-averaged and multicomponent diffusion models.

Acknowledgements

This material is based upon work supported by the National Science Foundation under Grant No. 1314109-DGE. This research used resources of the National Energy Research Scientific Computing Center (NERSC), a U.S. Department of Energy Office of Science User Facility operated under Contract No. DE-AC02-05CH11231.

References

- [1] N. Burali, S. Lapointe, B. Bobbitt, G. Blanquart, Y. Xuan, Assessment of the constant non-unity Lewis number assumption in chemically-reacting

- flows, *Combustion Theory and Modelling* 20 (4) (2016) 632–657. doi:
[10.1080/13647830.2016.1164344](https://doi.org/10.1080/13647830.2016.1164344).
- [2] R. B. Bird, W. E. Stewart, E. N. Lightfoot, *Transport Phenomena*, John Wiley & Sons, Inc., New York, 1960.
- [3] J. Warnatz, Calculation of the Structure of Laminar Flat Flames I: Flame Velocity of Freely Propagating Ozone Decomposition Flames, *Berichte der Bunsengesellschaft für physikalische Chemie* 82 (2) (1978) 193–200. doi:
[10.1002/bbpc.197800010](https://doi.org/10.1002/bbpc.197800010).
- [4] M. E. Coltrin, R. J. Kee, J. A. Miller, A Mathematical Model of Silicon Chemical Vapor Deposition, *Journal of The Electrochemical Society* 133 (6) (1986) 1206. doi:
[10.1149/1.2108820](https://doi.org/10.1149/1.2108820).
- [5] S. Lapointe, G. Blanquart, Fuel and chemistry effects in high Karlovitz premixed turbulent flames, *Combustion and Flame* 167 (2016) 294–307. doi:
[10.1016/j.combustflame.2016.01.035](https://doi.org/10.1016/j.combustflame.2016.01.035).
- [6] J. Schlup, G. Blanquart, Validation of a mixture-averaged thermal diffusion model for premixed lean hydrogen flames, *Combustion Theory and Modelling* 22 (2) (2018) 264–290. doi:
[10.1080/13647830.2017.1398350](https://doi.org/10.1080/13647830.2017.1398350).
- [7] T. P. Coffee, J. M. Heimerl, Transport algorithms for premixed, laminar steady-state flames, *Combust. Flame* 43 (1981) 273–289. doi:
[10.1016/0010-2180\(81\)90027-4](https://doi.org/10.1016/0010-2180(81)90027-4).
- [8] J. Warnatz, Influence of transport models and boundary conditions on flame structure, in: N. Peters, J. Warnatz (Eds.), *Numerical Methods in Laminar Flame Propagation*, Vol. 6 of *Notes on Numerical Fluid Mechanics*, Vieweg+Teubner Verlag, Wiesbaden, 1982, pp. 87–111.
- [9] A. Ern, V. Giovangigli, Impact of detailed multicomponent transport on planar and counterflow hydrogen/air and methane/air flames, *Combustion Science and Technology* 149 (1-6) (1999) 157–181. doi:
[10.1080/00102209908952104](https://doi.org/10.1080/00102209908952104).

- [10] H. Bongers, L. P. H. De Goey, The effect of simplified transport modeling on the burning velocity of laminar premixed flames, *Combust. Sci. Technol.* 175 (10) (2003) 1915–1928. doi:[10.1080/713713111](https://doi.org/10.1080/713713111).
- [11] Y. Xin, W. Liang, W. Liu, T. Lu, C. K. Law, A reduced multicomponent diffusion model, *Combust. Flame* 162 (1) (2015) 68–74. doi:[10.1016/j.combustflame.2014.07.019](https://doi.org/10.1016/j.combustflame.2014.07.019).
- [12] J. De Charentenay, A. Ern, Multicomponent transport impact on turbulent premixed H₂/O₂ flames, *Combust. Theor. Model.* 6 (3) (2002) 439–462. doi:[10.1088/1364-7830/6/3/304](https://doi.org/10.1088/1364-7830/6/3/304).
- [13] V. Giovangigli, Multicomponent transport in laminar flames, *Proceedings of the Combustion Institute* 35 (1) (2015) 625–637. doi:[10.1016/j.proci.2014.08.011](https://doi.org/10.1016/j.proci.2014.08.011).
- [14] G. Borghesi, J. Bellan, *A priori* and *a posteriori* investigations for developing large eddy simulations of multi-species turbulent mixing under high-pressure conditions, *Physics of Fluids* 27 (3) (2015) 035117. doi:[10.1063/1.4916284](https://doi.org/10.1063/1.4916284).
- [15] A. Ern, V. Giovangigli, Fast and Accurate Multicomponent Transport Property Evaluation, *Journal of Computational Physics* 120 (1) (1995) 105–116. doi:[10.1006/JCPH.1995.1151](https://doi.org/10.1006/JCPH.1995.1151).
- [16] A. Ern, V. Giovangigli, Thermal diffusion effects in hydrogen-air and methane-air flames, *Combust. Theor. Model.* 2 (4) (1998) 349–372. doi:[10.1088/1364-7830/2/4/001](https://doi.org/10.1088/1364-7830/2/4/001).
- [17] S. Ambikasaran, K. Narayanaswamy, An accurate, fast, mathematically robust, universal, non-iterative algorithm for computing multi-component diffusion velocities, *Proceedings of the Combustion Institute* 36 (1) (2017) 507–515. doi:[10.1016/j.proci.2016.05.055](https://doi.org/10.1016/j.proci.2016.05.055).
- [18] O. Desjardins, G. Blanquart, G. Balarac, H. Pitsch, High order conservative finite difference scheme for variable density low Mach number turbulent

- flows, *Journal of Computational Physics* 227 (15) (2008) 7125–7159. doi:
[10.1016/j.jcp.2008.03.027](https://doi.org/10.1016/j.jcp.2008.03.027).
- [19] B. Savard, Y. Xuan, B. Bobbitt, G. Blanquart, A computationally-efficient, semi-implicit, iterative method for the time-integration of reacting flows with stiff chemistry, *Journal of Computational Physics* 295 (2015) 740–769. doi:[10.1016/j.jcp.2015.04.018](https://doi.org/10.1016/j.jcp.2015.04.018).
- [20] J. O. Hirschfelder, C. F. Curtiss, R. B. Bird, *Molecular Theory of Gases and Liquids*, Wiley, New York, 1954.
- [21] C. F. Curtiss, J. O. Hirschfelder, Transport properties of multicomponent gas mixtures, *The Journal of Chemical Physics* 17 (6) (1949) 550–555. doi:[10.1063/1.1747319](https://doi.org/10.1063/1.1747319).
- [22] J. F. Grear, J. B. Bell, M. S. Day, The Soret effect in naturally propagating, premixed, lean, hydrogen-air flames, *Proceedings of the Combustion Institute* 32 (2009) 1173–1180. doi:[10.1016/j.proci.2008.06.075](https://doi.org/10.1016/j.proci.2008.06.075).
- [23] J. Schlup, G. Blanquart, A reduced thermal diffusion model for H and H₂, *Combustion and Flame* 191 (2018) 1–8. doi:[10.1016/j.combustflame.2017.12.022](https://doi.org/10.1016/j.combustflame.2017.12.022).
- [24] R. Kee, F. Rupley, J. Miller, *Chemkin-II: A Fortran chemical kinetics package for the analysis of gas-phase chemical kinetics*, Sandia National Laboratories Report SAND89-8009 (1989).
- [25] G. Dixon-Lewis, Flame structure and flame reaction kinetics. II. transport phenomena in multicomponent systems, *Proceedings of the Royal Society of London A: Mathematical, Physical and Engineering Sciences* 307 (1488). doi:[10.1098/rspa.1968.0178](https://doi.org/10.1098/rspa.1968.0178).
- [26] Y. Xuan, G. Blanquart, M. E. Mueller, Modeling curvature effects in diffusion flames using a laminar flamelet model, *Combustion and Flame* 161 (5) (2014) 1294–1309. doi:[10.1016/j.combustflame.2013.10.028](https://doi.org/10.1016/j.combustflame.2013.10.028).

- [27] Y. Xuan, G. Blanquart, Effects of aromatic chemistry-turbulence interactions on soot formation in a turbulent non-premixed flame, *Proceedings of the Combustion Institute* 35 (2) (2015) 1911–1919. doi:[10.1016/j.proci.2014.06.138](https://doi.org/10.1016/j.proci.2014.06.138).
- [28] Y. Xuan, G. Blanquart, Two-dimensional flow effects on soot formation in laminar premixed flames, *Combustion and Flame* 166 (2016) 113–124. doi:[10.1016/j.combustflame.2016.01.007](https://doi.org/10.1016/j.combustflame.2016.01.007).
- [29] P. L. Carroll, G. Blanquart, A proposed modification to Lundgren’s physical space velocity forcing method for isotropic turbulence, *Physics of Fluids* 25 (10) (2013) 105114. doi:[10.1063/1.4826315](https://doi.org/10.1063/1.4826315).
- [30] S. Verma, Y. Xuan, G. Blanquart, An improved bounded semi-Lagrangian scheme for the turbulent transport of passive scalars, *Journal of Computational Physics* 272 (2014) 1–22. doi:[10.1016/j.jcp.2014.03.062](https://doi.org/10.1016/j.jcp.2014.03.062).
- [31] M. E. Mueller, H. Pitsch, LES model for sooting turbulent nonpremixed flames, *Combustion and Flame* 159 (6) (2012) 2166–2180. doi:[10.1016/j.combustflame.2012.02.001](https://doi.org/10.1016/j.combustflame.2012.02.001).
- [32] F. Bisetti, G. Blanquart, M. E. Mueller, H. Pitsch, On the formation and early evolution of soot in turbulent nonpremixed flames, *Combustion and Flame* 159 (1) (2012) 317–335. doi:[10.1016/j.combustflame.2011.05.021](https://doi.org/10.1016/j.combustflame.2011.05.021).
- [33] B. Savard, G. Blanquart, Broken reaction zone and differential diffusion effects in high Karlovitz $n\text{-C}_7\text{H}_{16}$ premixed turbulent flames, *Combustion and Flame* 162 (5) (2015) 2020–2033. doi:[10.1016/j.combustflame.2014.12.020](https://doi.org/10.1016/j.combustflame.2014.12.020).
- [34] M. Herrmann, G. Blanquart, V. Raman, Flux Corrected Finite Volume Scheme for Preserving Scalar Boundedness in Reacting Large-Eddy Simulations, *AIAA Journal* 44 (12) (2006) 2879–2886. doi:[10.2514/1.18235](https://doi.org/10.2514/1.18235).

- [35] C. Pierce, Progress-variable approach for large-eddy simulation of turbulent combustion, Ph.D. thesis, Stanford University (2001).
- [36] L. Shunn, F. Ham, P. Moin, Verification of variable-density flow solvers using manufactured solutions, *Journal of Computational Physics* 231 (9) (2012) 3801–3827. doi:[10.1016/j.jcp.2012.01.027](https://doi.org/10.1016/j.jcp.2012.01.027).
- [37] O. Desjardins, G. Blanquart, G. Balarac, H. Pitsch, High order conservative finite difference scheme for variable density low Mach number turbulent flows, *Journal of Computational Physics* 227 (15) (2008) 7125–7159. doi:[10.1016/j.jcp.2008.03.027](https://doi.org/10.1016/j.jcp.2008.03.027).
- [38] R. D. Falgout, U. M. Yang, hypre: A Library of High Performance Preconditioners, in: P. M. A. Sloot, A. G. Hoekstra, C. J. K. Tan, J. J. Dongarra (Eds.), *Computational Science — ICCS 2002*, Springer, Berlin, Heidelberg, 2002, pp. 632–641. doi:[10.1007/3-540-47789-6_66](https://doi.org/10.1007/3-540-47789-6_66).
- [39] L. F. Richardson, The approximate arithmetical solution by finite differences of physical problems involving differential equations, with an application to the stresses in a masonry dam, *Philosophical Transactions of the Royal Society of London A: Mathematical, Physical and Engineering Sciences* 210 (459-470). doi:[10.1098/rsta.1911.0009](https://doi.org/10.1098/rsta.1911.0009).
- [40] F. Perini, E. Galligani, R. D. Reitz, A study of direct and Krylov iterative sparse solver techniques to approach linear scaling of the integration of chemical kinetics with detailed combustion mechanisms, *Combustion and Flame* 161 (5) (2014) 1180–1195. doi:[10.1016/j.combustflame.2013.11.017](https://doi.org/10.1016/j.combustflame.2013.11.017).
- [41] Z. Hong, D. F. Davidson, R. K. Hanson, An improved H₂/O₂ mechanism based on recent shock tube/laser absorption measurements, *Combustion and Flame* 158 (4) (2011) 633–644. doi:[10.1016/j.combustflame.2010.10.002](https://doi.org/10.1016/j.combustflame.2010.10.002).

- [42] K.-Y. Lam, D. F. Davidson, R. K. Hanson, A shock tube study of $\text{H}_2 + \text{OH} \rightarrow \text{H}_2\text{O} + \text{H}$ using OH laser absorption, *International Journal of Chemical Kinetics* 45 (6) (2013) 363–373. doi:10.1002/kin.20771.
- [43] Z. Hong, K.-Y. Lam, R. Sur, S. Wang, D. F. Davidson, R. K. Hanson, On the rate constants of $\text{OH} + \text{HO}_2$ and $\text{HO}_2 + \text{HO}_2$: A comprehensive study of H_2O_2 thermal decomposition using multi-species laser absorption, *Proceedings of the Combustion Institute* 34 (1) (2013) 565–571. doi:10.1016/j.proci.2012.06.108.
- [44] D. G. Goodwin, H. Moffat, K., R. L. Speth, *Cantera: An Object-oriented Software Toolkit for Chemical Kinetics, Thermodynamics, and Transport Processes, Version 2.3.0* (2017). doi:10.5281/zenodo.170284.
URL <https://www.cantera.org>
- [45] C. Rosales, C. Meneveau, Linear forcing in numerical simulations of isotropic turbulence: Physical space implementations and convergence properties, *Physics of Fluids* 17 (9) (2005) 095106. doi:10.1063/1.2047568.
- [46] F. A. Williams, *Combustion Theory*, Benjamin/Cummings, 1985.
- [47] M. Day, J. Bell, P. Bremer, V. Pascucci, V. Beckner, M. Lijewski, Turbulence effects on cellular burning structures in lean premixed hydrogen flames, *Combust. Flame* 156 (5) (2009) 1035–1045. doi:10.1016/j.combustflame.2008.10.029.
- [48] A. J. Aspden, M. S. Day, J. B. Bell, Turbulence-flame interactions in lean premixed hydrogen: Transition to the distributed burning regime, *J. Fluid Mech.* 680 (2011) 287–320. doi:10.1017/jfm.2011.164.
- [49] A. Aspden, M. Day, J. Bell, Turbulence-chemistry interaction in lean premixed hydrogen combustion, *Proc. Combust. Inst.* 35 (2) (2015) 1321–1329. doi:10.1016/j.proci.2014.08.012.

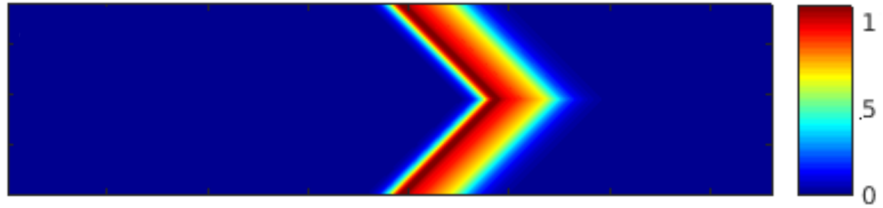
- [50] Y. He, B. Cook, J. Deslippe, B. Friesen, R. Gerber, R. Hartman-Baker, A. Koniges, T. Kurth, S. Leak, W.-S. Yang, Z. Zhao, E. Baron, P. Hauschildt, Preparing NERSC users for cori, a cray XC40 system with intel many integrated cores, *Concurrency and Computation: Practice and Experience* 30 (1) (2017) e4291. [doi:10.1002/cpe.4291](https://doi.org/10.1002/cpe.4291).

Appendix A. Method verification

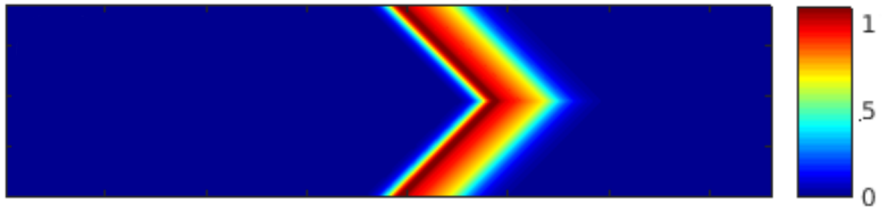
To verify the method implementation, we generated an artificial species profile where the direction and relative magnitudes of the flux vectors could be predicted a priori remain independent of any preferential diffusion effects that may exist in a physical system. Specifically, we created a two-dimensional V-shaped species profile with a central angle of 45° and projected it into three dimensions as shown in Figure A.14a.

Such a profile results in flux vectors that are constant in the y -direction, of equal magnitude and opposite sign in the z -direction reflected over the x - y -plane, and vary in magnitude but remain constant in sign matching the initial input profile in the x -direction. These predictions should be consistent independent of chemical species or other scalar value for the artificial input profile. We ran the algorithm for one “complete” set of subiterations to convergence and normalized the resulting diffusion flux vectors to ensure the relative magnitudes and direction were consistent with our expectations.

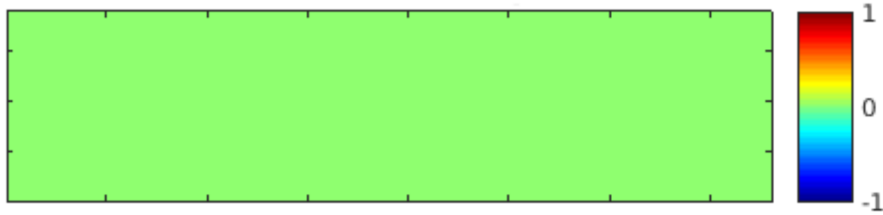
Figure A.14 shows the results of this artificial test case. The resulting normalized flux vectors agree with expectation and have equal magnitudes in the x - and z -directions corresponding to the 45° artificial flame angle. This result indicates proper functionality of the proposed method.



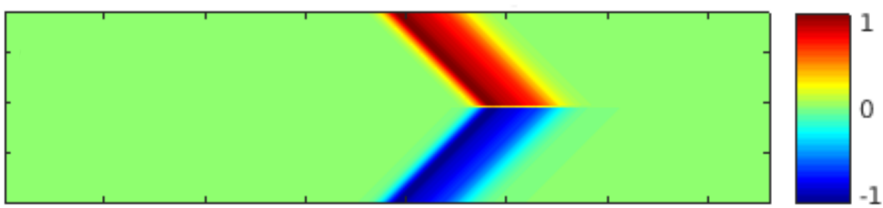
(a) Input species profile



(b) x -component of mass flux



(c) y -component of mass flux



(d) z -component of mass flux

Figure A.14: Normalized flux vectors resulting from an artificial species profile after one full iteration of semi-implicit multicomponent diffusion calculation.